Nd-doped Upconverting Nanoparticles for Deep Tissue Imaging

Hugo Söderlund
June 19, 2014

Master Thesis

LUND
UNIVERSITY

Advisors

Prof. Stefan Andersson-Engels, Division of Atomic Physics, Lund University, Lund, Sweden
Ph.D. Haichun Liu, Division of Atomic Physics, Lund University, Lund, Sweden
Ph.D. Can T. Xu, Division of Atomic Physics, Lund University, Lund, Sweden

Examiner

Prof. Hans Lundberg, Division of Atomic Physics, Lund University, Lund, Sweden

Nd-doped Upconverting Nanoparticles for Deep Tissue Imaging

Populärvetenskaplig Sammanfattning

I dagens sjukvård används ett flertal olika metoder för att undersöka insidan av kroppen, såsom magnetisk resonanstomografi (MRT) eller röntgen. De har båda fördelar och nackdelar, t.ex. är MRT dyrt och tar lång tid men är väldigt noggrant och är inte begränsad i hur djupt avbildningen kan ske. En annan metod, som använder sig av optiska markörer för att undersöka kroppen, är fluorescenstomografi.

Fluorescens uppkommer när en ljusfoton absorberas av en atom eller molekyl så att denna hamnar i ett exciterat tillstånd. Den exciterade molekylen skickar sedan ut sin energi i form av en ny foton med lägre energi än den inkommande fotonen pga energiomvandlingar med förluster. Den utsända fotonen kallas fluorescensljus. Fluorescens används inom ett flertal områden som inkluderar lysrör, markering i sedlar och medicin. Inom biomedicin kan man använda sig av fluorescerande markörer för detektion. Ofta behandlas markören med ett enzym som söker sig till önskad vävnad, t.ex. tumörer, och därmed får man målsökande fluoroforer som kan injiceras i kroppen. När man sedan belyser områden som önskas undersökas kan man detektera var tumören är lokaliserad genom att analysera den fluorescerande signalen.

Fördelarna med en sådan här detektion är att den är snabb och billig jämfört med andra detektionsmetoder. Nackdelarna är att excitationsljuset ofta har svårt att nå djupt i biologisk vävnad samt att fluorescens även uppstår i övrig vävnad, s.k. autofluorescens. Då vävnadens autofluorescens liksom den tumörsökande fluoroforen emitterar fotoner, kommer fluoroforens signal överlappa autofluorescensen. Detta medför en dålig kontrast mellan signal och bakgrund. Ett sätt att undgå detta problem är att använda sig av uppkonverterande nanopartiklar som fluoroforer. Uppkonversion innebär att två eller fler fotoner absorberas för att emittera en foton med högre energi än det inkommande ljuset. Därmed kommer den uppkonverterade signalen hamna i ett våglängdsområde där det inte förekommer någon autofluorescens.

Uppkonverterande nanopartiklar, som har använts i den här rapporten, är uppbyggda av sällsynta jordartsmetaller som gemensamt uppkonverterar ljuset. Beroende på vilka sällsynta jordartsmetaller

som används kan excitations- samt emissionsvåglängden ändras. En väl använd och analyserad kombination är med ytterbium (Yb) och thulium (Tm). Denna kombination skapar uppkonverterande nanopartiklar med excitationsvåglängd vid 975 nm samt emissionsvåglängd vid 800 nm. Detta är en väl fungerande kombination, men i biologisk vävnad har vatten en relativt hög absorption vid just 975 nm. Detta medför att excitationsljuset snabbt absorberas vid djupare mätningar. En ny kombination av sällsynta jordartsmetaller har konstruerats av neodymium (Nd), ytterbium (Yb) samt erbium (Er), för att skifta excitationsljuset från 975 nm till 808 nm med effektivt emissions-ljus vid 650 nm. Fördelen med excitation vid 808 nm jämfört med 975 nm är att vattens absorption är lägre vid 808 nm. Då biologisk vävnad till största del består av vatten kommer detta leda till möjlighet att erhålla signal vid större djup. I denna uppsats har jämförelse mellan Yb^{3+}/Tm^{3+} och $Nd^{3+}/Yb^{3+}/Er^{3+}$ uppkonverterande nanopartiklar gjorts i vävnadsfantomer för att beskriva fördelen med 808 nm excitationsljus vid olika djup. Det påvisas både experimentellt och med simuleringar att signalen dämpas mindre för stora djup med de nya partiklarna, och medför därmed en möjlighet för en ny, förbättrad optisk markör för tillämpningar inom biomedicin.
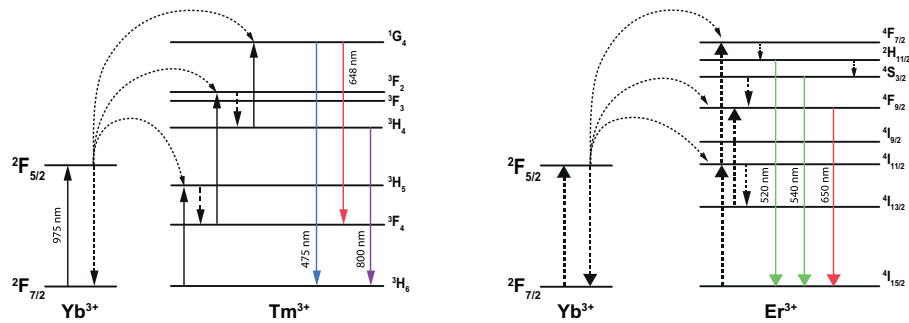
Energinivåstruktur för de signifikanta överföringarna i de två använda partiklarna, Yb/Tm till vänster samt (Nd)/Yb/Er till höger. Som synes krävs två eller fler fotoner för att uppnå uppkonversion. Då emissionsljuset utsänds med en högre energi än inkommande excitationsljus, kan signalen detekteras utan att påverkas av vävnadens autofluorescens.

List of Abbreviations

CT	computed tomografy
CW	continuous wave
ESA	excited state absorption
ETU	energy transfer upconversion
MC	Monte Carlo
MRI	magnetic resonance imaging
PTOF	photon time of flight
RE	rare earth
RTE	radiative transfer equation
r.u.	relative units
UC	upconversion
UCNP	upconverting nanoparticle

Abstract

During the last decade, upconverting nanoparticles (UCNPs) doped with rare-earth (RE) ions have been extensively studied in the field of biophotonics. Due to their unique properties of anti-Stokes shifted luminescence and with excitation and emission wavelengths optimal for biomedical imaging, they have become an interesting class of fluorescent contrast agents. An issue with down-converting fluorescent contrast agents for imaging in tissue is the inevitable autofluorescence that overlaps the signal from the added fluorophore, limiting the signal-to-background ratio. With UCNPs it is possible to achieve a near autofluorescence free signal due to their upconverting nature.

Up to date, one of the most efficient UCNPs is the Yb^{3+}/Tm^{3+} $NaYF_4$ UCNPs. With an excitation wavelength of 975 nm and emission at 800 nm they operate in the diagnostics window (600 - 1200 nm), allowing for substantial tissue penetration. Unfortunately, water has an absorption peak at 975 nm, leading to a loss in penetration depth as well as heat produced in the tissue. Very recently, Nd^{3+}/Yb^{3+} co-sensitized UCNPs have been synthesized, tuning the excitation wavelength to 808 nm. With a lower water absorption at 808 nm the new co-sensitized UCNPs are proposed to gain in penetration depth as well as reduce heat production in tissue. This thesis explores the advantages of using the newly proposed UCNPs as compared to Yb^{3+}/Tm^{3+} UCNPs. By using tissue phantoms with realistic optical properties, the penetration depth as well as the signal loss was evaluated experimentally. Additionally, simulations were performed in order to further explore the benefits of the new particles. Based on the results presented in this work, the new UCNPs may very well replace the traditional particles for certain applications, and may lead us one step closer to finding the optimal tools for biomedical applications.

Contents

Introduction

Common medical imaging methods involve X-ray Computed Tomography (CT), Ultrasound and Magnetic Resonance Imaging (MRI). These methods all have benefits in different situations, but also some drawbacks. MRI, as an example, has excellent imaging depth and spatial resolution, but equipment comes at a high cost and data acquisition takes a long time. Optical imaging, with its low costs and fast acquisition times in addition to safe radiation, is a promising addition to the current imaging methods. For fluorescence molecular imaging, contrast agents are of great importance, as they determine what is reported from the biological area of interest. These contrast agents may be either natural chromophores in the body [1], or externally added in order to choose the spectroscopic properties. Most of the externally added contrast agents exhibit natural Stokes-shifted emission, i.e. with a lower energy emission compared to incoming light, which is spectrally similar to the tissue autofluorescence. This causes the signal from the contrast agents to be covered by the autofluorescence, limiting the detection sensitivity. With recent development of upconverting nanocrystals as contrast agents it is possible to overcome the issue of autofluorescence [2]. UCNPs are nanosized crystals containing rare earth (RE) ions set up as sensitizers and activators. This combination allows for upconversion of light, leading to an anti-Stokes shifted emission that will be spectrally separated from the autofluorescence. These unique properties, along with other benefits, makes it possible to receive an increased signal-to-noise ratio compared to using regular fluorophores. Furthermore, by choosing the RE ions wisely, the UCNPs can be tuned to optimal excitation and emission wavelengths for optical imaging.

1.1 Obstacles to Overcome

The UCNPs have been immensely studied in the field of biophotonics, with applications such as *in vitro* cancer cell imaging, *in vivo* tumor targeting imaging, photodynamic therapy and fluorescence diffuse optical tomography [3], to mention a few. One of the first observed and efficient upconverting nanocrystals are the ytterbium Yb^{3+}/Tm^{3+}-$NaYF_4$. As stated by Auzel, "... as is often in science, the most efficient systems are the ones discovered at first, here the Yb-Er and the Yb-Tm systems." [4]. However, despite its efficiency, these traditional UCNPs have an excitation wavelength at 975 nm, where water has

a relatively strong absorption. This causes both heat generation in tissue and loss of excitation light, which leads to a poor penetration depth for biomedical applications.

1.2 Aims of the Thesis

Studies using a continuous wave (CW) laser with a wavelength of 915 nm to excite Yb^{3+}/Tm^{3+} has been reported by Zhan *et al.* [3]. Thus, the absorption from water is significantly reduced compared to 975 nm, and great results in both reduced heat generation and increased tissue penetration depth were reported. However, recently discovered $Nd^{3+}/Yb^{3+}/Er^{3+}$ co-sensitized nanocrystals with an excitation wavelength at 808 nm and emission wavelength at 650 nm have been introduced, allowing for an even further decrease in water absorption. These newly developed co-sensitized UCNPs have never before been experimentally compared with the traditional Yb^{3+}/Tm^{3+} UCNPs, with the goal of reaching larger penetration depths. Such experiments have been conducted for this thesis. In addition, different compositions of tissue phantoms were simulated in order to find the optimal parameters for depth penetration with the new particles. The experiments and the corresponding results and conclusions will be discussed in this thesis.

Outline of the Thesis

The subsequent chapters will contain the following:

Chapter 2 will focus on tissue optics. Here, a general theory of light and light interaction with biological tissue is considered, such as absorption, scattering and luminescence. Furthermore, a description of how light can be modeled in biological tissue, including the radiative transfer equation (RTE), the diffusion approximation and Monte Carlo simulations are discussed.

Chapter 3 contains a description of the UCNPs, their upconversion mechanisms and the particles that were used in this work. Additionally, a discussion of how to choose the host materials along with the activator and sensitizer ions are included, with a final remark of future outlooks in the area.

Chapter 4 provides a thorough experimental description, including practical measurements, materials used as well as simulations performed and finally a discussion of the results.

Chapter 5 is the final chapter, where concluding remarks and final thoughts are presented, along with outlooks for the future and a personal reflection.

Tissue Optics

For biomedical applications it is essential to know the tissue characteristics in order to find optimal tools to work with. Most biological tissues are characterized by strong optical scattering, and are thus referred to as *scattering* or *turbid media* [5]. Light that interacts with tissue will also be absorbed depending on the absorbing components in tissue, i.e. the chromophores. In this chapter, an overview of tissue optics will be presented, including absorption and scattering as well as common chromophores in biological tissue. Finally, some of the most commonly used expressions of light distribution in media will be derived.

2.1 Absorption

An important parameter in tissue optics is absorption. It can be seen from a classical electromagnetic point of view in the following way: when light radiates on matter composed of discrete electrical charges, these electrical charges will be forced to oscillate in the same frequency as the incident electric field. If the natural frequency of the molecules are in resonance with the incoming frequency from the electric field, energy will be transferred to the system, increasing the amplitude of the vibration. Most often, the lifetime of the excited state is higher than the collision rate of the molecules, raising the kinetic energy of other molecules in the system. Thus, the energy is often anticipated as heat in the medium. This process is known as absorption [6]. For a single atom or molecule the probability of absorption is described by the cross section σ_{abs} [cm^2] of the absorber. The absorption coefficient μ_a [cm^{-1}], which describes the absorption probability per unit path length of light in the medium, can thus be described by the contribution from all the absorbers in the medium [5]

$$\mu_a = N_{abs}\sigma_{abs}, \tag{2.1}$$

here N_{abs} [cm^{-3}] describes the number density of the identical absorbers. For biological tissue there are several kinds of absorbers (or chromophores), which will be discussed a bit more in detail later. For a medium with several kinds of chromophores, the absorption coefficient is thus the sum of the contribution from every chromophore

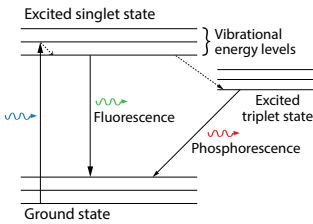$$\mu_a = \sum_i N_i\sigma_i, \tag{2.2}$$

and may also be written as

$$\mu_a = \sum_i V_i \mu_i, \qquad (2.3)$$

where V_i [%] is the volume fraction of the chromophore and μ_i [cm^{-1}] is the absorption coefficient of the chromophore in its pure form.

When light travels through absorbing media the intensity of the light will decrease. A well known expression for how the intensity decreases over optical path length is the Beer-Lambert-Bouguer law [7]

$$I = I_0 e^{-\mu_a \cdot l}, \qquad (2.4)$$

where I [W/cm^2] is the transmitted intensity, I_0 [W/cm^2] is the initial intensity and l [cm] is the distance traveled through the absorbing medium.

2.2   Luminescence

Absorption of a photon may excite an electron in a molecule from the ground state to an excited state. From the excited state, there are several possible outcomes. The energy may be released non-radiatively from the excited state in the form of heat or another photon may be released, i.e. *luminescence*. Luminescence is a collective term for *fluorescence* and *phosphorescence*. Fluorescence occurs with a transition between singlet states in molecules, while phosphorescence includes an intersystem crossing to a triplet state before emission to a singlet state occurs [8]. Due to the violation of the transition selection rule for phosphorescence, this phenomena has a lower probability and a longer lifetime than fluorescence. In common for both deexcitation mechanisms is that the energy is partly released non-radiatively through vibrational relaxation to the lowest vibrational energy level in the excited state, to eventually be released as a photon [5]. This causes the energy of the emitted photon to have a lower energy than the absorbed photon, i.e. the emission is *Stokes-shifted*. Figure (2.1) shows a Jablonski energy diagram, illustrating both fluorescence from the singlet state, and phosphorescence after an intersystem crossing to a triplet state.

Figure 2.1:   Jablonski energy diagram including absorption to a singlet state, fluorescence back to the ground state, and phosphorescence after an intersystem crossing to a triplet state.

2.3   Scattering

Another important parameter for understanding light propagation through tissue is light scattering. Scattering causes the direction of the photons to diverge from their original direction in the medium. The phenomena can be described in an electromagnetic point of view; charged particles that are set in oscillatory motion by an incoming electric field, and re-emit light of the same frequency as the incoming wave, is known as light scattering [9].

If scatterers are sparsely distributed in a medium i.e. the mean distance between particles is much greater than both the scatterer size and the wavelength, single scattering can be considered. If this is not the case, the medium is considered to be densely packed and each scatterer does not affect propagation independently. In the case of single scattering, a single particle is assumed for each scattering event and the size and shape are of fundamental importance in determining the scattered field. Lord Rayleigh studied particles much smaller

than the incoming wavelength and described the scattering cross section σ_{sca} [cm^2] as [10]

$$\sigma_{sca}^{Ray} \propto \lambda^{-4}, \tag{2.5}$$

where λ [nm] denotes the wavelength of the light. A more advanced description is that of Mie, where both number density and size of the scatterers are taken into account [11]

$$\sigma_{sca}^{Mie} \propto a\lambda^{-b}, \tag{2.6}$$

where a and b are coefficients dependent on the amount of scatterers and the size, respectively.

When it is considered a loosely packed medium the scatterer number density over volume N_{sca} [cm^{-3}] and their independent scattering coefficient σ_{sca} give an expression of the total scattering coefficient μ_s [cm^{-1}]

$$\mu_s = N_{sca}\sigma_{sca}, \tag{2.7}$$

where μ_s is defined as the probability of photon scattering per unit path length of light in the medium. The reciprocal of μ_s is considered the scattering *mean free path*, i.e. the distance between two scattering events [5].

2.4 Henyey-Greenstein Phase Function

Henyey and Greenstein (1941) created an expression which describes the angular dependence of scattered light by small particles. It is known as the Henyey-Greenstein phase function [12] and has been proven to be useful for approximating the angular scattering dependence of single scattering events in biological tissue. The function allows variation of the anisotropy factor $-1 \leq g \leq 1$ to determine the probability of the direction of the scattering, θ as

$$p(\theta) = \frac{1}{4\pi} \frac{1-g^2}{[1+g^2-2g\cos(\theta)]^{3/2}}. \tag{2.8}$$

To get a feeling for what the values of the anisotropy factor determine, one can assume two extreme values of θ: forward scattering with $\theta = 0$ and back scattering with $\theta = \pi$. The probability for forward scattering is $p(0) = \frac{1-g^2}{4\pi(1-g)^3}$ and for back scattering $p(\pi) = \frac{1-g^2}{4\pi(1+g)^3}$. The ratio of forward scattering over back scattering hence becomes $[(1+g)/(1-g)]^3$ where it is noticable that for $g > 0$, forward scattering is dominant, and for $g < 0$ back scattering is dominant. In Figure (2.2) the phase function can be seen for different values of the anisotropy factor.

The anisotropy factor describes the expectation value of the direction for a scattered photon, and is often used in combination with the scattering coefficient μ_s to describe the *reduced scattering coefficient, $\mu_s' = \mu_s(1-g)$*. The purpose is to describe the diffusion of photons in a random walk with step size $1/\mu_s'$ which is equivalent to many small steps of *mean free path* $1/\mu_s$ with corresponding expected scattering angles [13], as can be seen in Figure (2.3).

2.5 Chromophores

The human and animal body is built up on several important components in order for us to function properly. Many of these absorb light and hence go
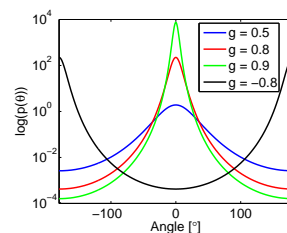
Figure 2.2: Henyey-Greenstein phase function for $g = 0.9, g = 0.8, g = 0.5$ and $g = -0.8$.
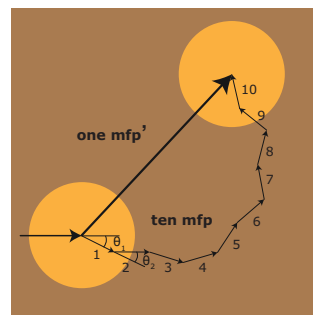
Figure 2.3: The equivalence of taking ten smaller steps of *mean free path* with anisotropic deflection angles and one big step with a *reduced mean free path*.
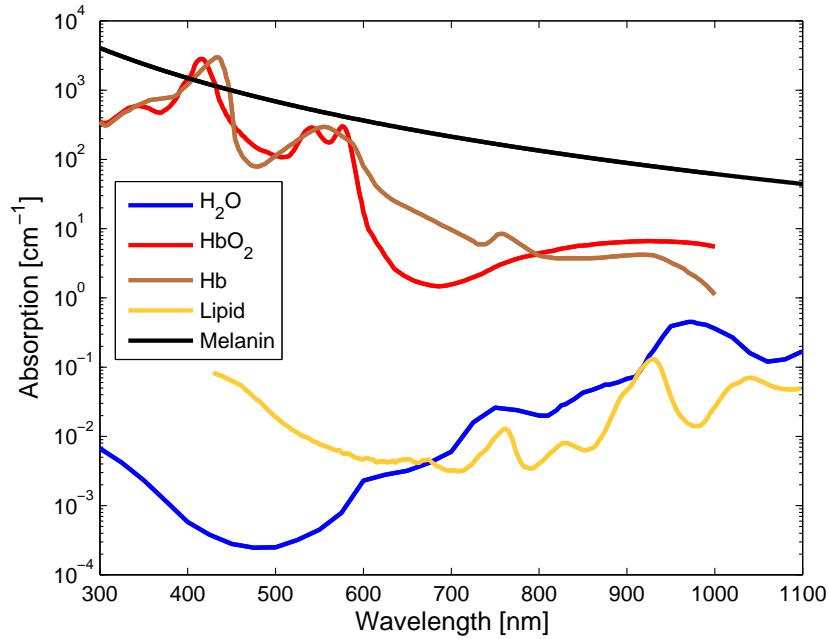
Figure 2.4: Absorption coefficients for the main chromophores in biological tissue. The absorption coefficients of the chromophores (except for melanin) are represented in their pure form, i.e. a volume fraction of 100%.

under the name chromophore. Typical chromophores in biological tissue are water, blood, lipid and melanin. The absorption coefficients as a function of wavelength can be seen in Figure (2.4). The values are taken from various articles, [14] [15] [16] [17].

Water

Since our bodies contain 60-70% water [3], the absorption of water will have a huge impact on light transportation in our bodies. The blue line in Figure (2.4) shows the light absorption for water as a function of wavelength. The water absorption peak at 975 nm will be discussed later on in this work.

Haemoglobin

The second chromophore, haemoglobin comes in two forms; oxygenated (HbO_2) and deoxygenated (Hb). Since blood is constantly delivering oxygen to the cells in the body it will contain different amounts of oxygen depending on where in the body it is measured. The amount of oxygenated over deoxygenated blood is described by the blood oxygenation or blood saturation [%]. A normal saturation value is around 70 % [18].

Lipid

Lipids are fat particles that exist in subcutaneous tissue and around organs. The orange line in Figure (2.4) shows an absorption spectrum of pig lard measured by van Veen *et al.* and was reported to match the measured spectrum of lipid in mammalian tissue [19].

Melanin

Melanin is the pigment found in the epidermal layer of human skin. It has a large scattering coefficient in the ultraviolet region which protects us from harmful UV-light. The black line in Figure (2.4) is a general shape that approximates the melanosome absorption spectrum in skin as

$$\mu_a = 1.70 \cdot 10^{12} \left(\frac{\lambda}{1nm} \right)^{-3.48}. \tag{2.9}$$

Here, λ [nm] is the wavelength of interest and μ_a has the unit [cm^{-1}] [20]. It is clear that the absorption is reduced for higher wavelengths, however still large compared to other chromophores.

Biological tissue contains different amounts of above mentioned and other chromophores, which causes a certain set of wavelengths to be considered optimal for tissue penetration. Taking both absorption and scattering into account, the optical window is determined to be in the range 600-1200 nm [21].

2.6 Tissue Autofluorescence

Biological tissue contains several molecules that are natural fluorophores with a Stokes-shifted (lower energy than incoming light) emission light. In some cases, autofluorescence can be used to extract information about the morphological and physiological state of cells and tissue [1]. However, in most imaging and tomography techniques this causes more inconveniences than advantages. By adding a fluorophore with Stokes-shifted emission as a contrast agent into biological tissue, the signal will be superimposed on the tissue autofluorescence. Separating the two with an optical filter is not trivial since they are in the same spectral region. A time resolved imaging microscopy has been proposed [22], where the short decay time of the autofluorescence is exploited. By using a short light pulse and detecting the emission signal after a delay, one can retrieve a signal with reduced autofluorescence. While this is possible, it will require accurate time measurements and will also cause a loss in signal. Another, and relatively newly discovered method, is to use upconverting fluorescence markers that causes an anti-Stokes shift (higher energy fluorescence light than incoming light) upon NIR excitation. This causes the signal to be spectrally separated from the autofluorescence and can thus easily be obtained by using optical filters to block the noise.

2.7 Light Propagation in Tissue

The fundamental physics behind absorption and scattering of light radiation along with the major components responsible for these phenomena in biological

tissue has been described above. In order to describe how light propagates in
tissue, further tools are required. In this section, a model of light propagation
in tissue is described followed by methods for approximating and solving that
model. For the following arguments, it is referred to the work of *Wang* and
Wu [5], if nothing else is stated.

2.7.1 Radiative Transfer Equation

Light propagation in tissue can be described using Maxwell's electromagnetic
theory [23], but solutions will be very difficult to achieve due to the com-
plex nature of biological tissue. Another way to describe light propagation in
tissue is with the radiative transfer equation (RTE), which discards the elec-
tromagnetic wave theory and instead describes the photons as a flow of neutral
particles that can be absorbed or scattered. This allows for practical analytical
computations that accurately describes the photon transport in tissue.

The RTE is an analytical model of the energy transport by photons inside
media. It is fundamentally equal to the Boltzmann equation and can be derived
from the principle of conservation of energy. Briefly, the RTE takes into account
that energy from the beam of light is lost if a photon is absorbed or scattered
away from the beam and gains energy from light sources in the medium or
if a photon is scattered into the beam. The RTE is a differential equation
describing radiance, $L(\mathbf{r}, \hat{\mathbf{s}}, t)$ [W/m^{2}sr], defined as energy flow per unit normal
area per unit solid angle per unit time, with $\mathbf{r}$, $\hat{\mathbf{s}}$ and t describing position, unit
direction and time, respectively.

By considering a small volume V the RTE is described by four contributions;
divergence, extinction, scattering and sources in the volume.

1. The photon transfer across the boundary caused by divergence out of the
   volume element per unit time is described as

   $$dP_{div} = \hat{\mathbf{s}} \cdot \nabla L(\mathbf{r}, \hat{\mathbf{s}}, t)d\Omega dV, \qquad (2.10)$$

   where $d\Omega$ is the differential solid angle element along direction $\hat{\mathbf{s}}$.

2. The energy lost due to absorption and scattering within the solid angle
   element is given by

   $$dP_{ext} = (\mu_s + \mu_a)ds[L(\mathbf{r}, \hat{\mathbf{s}}, t)dAd\Omega], \qquad (2.11)$$

   with $(\mu_s + \mu_a)ds$ representing the probability of scattering and absorption
   in the volume length.

3. The scattering from any direction $\hat{\mathbf{s}}'$ into $d\Omega$ around direction $\hat{\mathbf{s}}$ per unit
   time is described by

   $$dP_{sca} = (\mu_s dV)[\int_{4\pi} L(\mathbf{r}, \hat{\mathbf{s}}', t)P(\hat{\mathbf{s}}' \cdot \hat{\mathbf{s}})d\Omega']d\Omega, \qquad (2.12)$$

   where $P(\hat{\mathbf{s}}' \cdot \hat{\mathbf{s}})$ represents the probability of light propagating from di-
   rection $\hat{\mathbf{s}}'$ being scattered into $d\Omega$ around direction $\hat{\mathbf{s}}$. The function is
   normalized, meaning it satisfies $\int_{4\pi} P(\hat{\mathbf{s}}' \cdot \hat{\mathbf{s}})d\Omega = 1$

4. The energy produced by a source in the volume element dV within the solid angle per unit time is given by

$$dP_{src} = S(\mathbf{r}, \hat{\mathbf{s}}, t)dV\,d\Omega, \tag{2.13}$$

with S carrying the unit $[\text{W/m}^3\text{sr}]$.

Finally, the change in energy in the volume element, dV, within the solid angle $d\Omega$ per unit time is

$$dP = \frac{\partial L(\mathbf{r}, \hat{\mathbf{s}}, t)/c}{\partial t}dV\,d\Omega. \tag{2.14}$$

Here, c denotes the speed of light in the medium. The principle of conservation of energy requires

$$dP = -dP_{div} - dP_{ext} + dP_{sca} + dP_{src}, \tag{2.15}$$

which, by substituting equations (2.10) - (2.14) into (2.15) gives

$$\frac{\partial L(\mathbf{r}, \hat{\mathbf{s}}, t)/c}{\partial t} = -\hat{\mathbf{s}}\cdot\nabla L(\mathbf{r}, \hat{\mathbf{s}}, t) - (\mu_s+\mu_a)L(\mathbf{r}, \hat{\mathbf{s}}, t) + \mu_s\int_{4\pi} L(\mathbf{r}, \hat{\mathbf{s}}', t)P(\hat{\mathbf{s}}'\cdot\hat{\mathbf{s}})d\Omega' + S(\mathbf{r}, \hat{\mathbf{s}}, t), \tag{2.16}$$

which is the RTE.

Solving the RTE analytically is not trivial. It is possible for simple one-dimensional cases, but for more complex situations approximations or numerical methods are required. A very popular approach in tissue optics is the diffusion approximation [24]. Another way is to numerically model light propagation in tissue using Monte Carlo simulations, which is a discrete version of the RTE [25]. These two methods have mainly been used in this thesis.

2.7.2 Diffusion Approximation

In the diffusion approximation the radiance, source term and phase functions are the first-order approximation of a spherical harmonic expansion, also known as the P_1 approximation. From here, a few assumptions are made in order to obtain the diffusion equation. First, the definitions of fluence, $\phi(\mathbf{r}, t)$ $[\text{Wm}^{-2}]$, and flux, $\mathbf{J}(\mathbf{r}, t)$ $[\text{Wm}^{-2}]$ are defined as

$$\phi(\mathbf{r}, t) = \int_{4\pi} L(\mathbf{r}, \hat{\mathbf{s}}, t)d\Omega, \tag{2.17}$$

and

$$\mathbf{J}(\mathbf{r}, t) = \int_{4\pi} L(\mathbf{r}, \hat{\mathbf{s}}, t)\hat{\mathbf{s}}d\Omega. \tag{2.18}$$

In the P_1 approximation the radiance can be expressed in terms of fluence and flux, as

$$L(\mathbf{r}, \hat{\mathbf{s}}, t) \approx \frac{1}{4\pi}\phi(\mathbf{r}, t) + \frac{3}{4\pi}\mathbf{J}(\mathbf{r}, t)\hat{\mathbf{s}}. \tag{2.19}$$

The source is assumed to be isotropic, i.e. independent of $\hat{\mathbf{s}}$, giving

$$S(\mathbf{r}, \hat{\mathbf{s}}, t) = \frac{S(\mathbf{r}, t)}{4\pi}. \tag{2.20}$$

Inserting equation (2.19) and (2.20) into the RTE, (2.16), and integrating over the full 4π solid angle yields two coupled equations

$$\left(\frac{1}{c}\frac{\partial}{\partial t} + \mu_a\right)\phi + \nabla\mathbf{J} = S(\mathbf{r}, t), \tag{2.21}$$

$$\left(\frac{1}{c}\frac{\partial}{\partial t} + \mu_a + \mu_s'\right)\mathbf{J} + \frac{1}{3}\nabla\phi = 0. \tag{2.22}$$
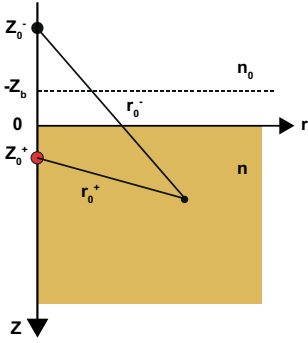
The second assumption is that the temporal change in flux is negligible, i.e. $\frac{\partial\mathbf{J}}{\partial t} = 0$, leading to

$$\mathbf{J} = -\frac{1}{3(\mu_a + \mu_s')}\nabla\phi = -D\nabla\phi, \tag{2.23}$$

which is known as *Fick's law*, with the parameter D [m] referred to as the diffusion coefficient, defined $D = \frac{1}{3(\mu_a + \mu_s')}$. Finally, by inserting equation (2.23) into (2.21) the diffusion equation is obtained

$$\frac{1}{c}\frac{\partial\phi(\mathbf{r}, t)}{\partial t} - \nabla D(\mathbf{r})\nabla\phi(\mathbf{r}, t) + \mu_a\phi(\mathbf{r}, t) = S(\mathbf{r}, t). \tag{2.24}$$

Along with the assumptions that the source is isotropic and that the temporal change in flux is negligible, the scattering must dominate over absorption in order for the diffusion approximation to be valid. While this is true for many biological applications, one might consider using a different approach, such as the numerical Monte Carlo method in order to get correct results.

Solutions to the Diffusion Equation

Compared to the RTE, the diffusion approximation can be analytically solved for certain geometries and cases. For a homogeneous and infinite medium the solution is found by the Green's functions. By assuming a point source, the Green's function for a steady state condition is

$$G(\mathbf{r}) = \frac{1}{4\pi D}\frac{e^{-\mu_{eff}\mathbf{r}}}{\mathbf{r}}, \tag{2.25}$$

with

$$\mu_{eff} = \sqrt{\mu_a/D}. \tag{2.26}$$

For a point source of power P_0 [W] the fluence rate distribution through the media can be expressed as

$$\phi = P_0 G. \tag{2.27}$$

The practical use for this approximation is limited due to the requirements needed for it to be accurate. However, it gives a simple solution to a complex problem and a visualization of how fluence is distributed in highly scattering tissue can easily be obtained. For a semi-infinite or slab geometry the fluence distribution can be described by using mirrored sources [8], see Figure (2.5). The real point source is located at $z_0^+ = 1/\mu_s'$ and is mirrored by the extrapolated boundary, i.e. the virtual boundary, separated from the real boundary by $z_b = 2AD$. The parameter A describes the refractive index mismatch at the boundary, derived by using Robin-type boundary conditions. Finally, this

Figure 2.5: Solving the diffusion approximation for a homogeneous medium with a semi-infinite geometry.

leads to a mirrored negative point source at a position $z_0^- = -z_0^+ - 2z_b$. The Green's function in steady state thus becomes

$$G(\mathbf{r}) = \frac{1}{4\pi D} \left(\frac{e^{-\mu_{eff}\mathbf{r}_0^+}}{\mathbf{r}_0^+} - \frac{e^{-\mu_{eff}\mathbf{r}_0^-}}{\mathbf{r}_0^-} \right), \tag{2.28}$$

with

$$\mathbf{r}_0^+ = \sqrt{r^2 + (z - z_0^+)^2}, \tag{2.29}$$

$$\mathbf{r}_0^- = \sqrt{r^2 + (z - z_0^-)^2}. \tag{2.30}$$

2.7.3 Monte Carlo Simulations

The Monte Carlo method is a way to numerically solve the RTE. The trajectory of a single photon is modeled, with the direction of each step depending on the previous step. By simulating a large number of photons physical quantities of the medium such as fluence, can be estimated for any given geometry [5]. Using a predetermined medium with given parameters μ_a, μ_s, and g the fate of a single photon is determined using random variables. The process uses the following scheme; a package of photons with an initial weight is launched into the medium and travels in a stepwise manner. For every step, its weight, position and direction will be influenced by the interactions between the photon package and the medium, including absorption, scattering, internal reflection and transmittance [26]. Finally, the particle is terminated and the simulations start over until all photon packages are simulated. For a large amount of simulations this will give a good statistical value of the light distribution in the chosen medium. However, more simulations leads to time consuming computations, which is the biggest limitation to Monte Carlo simulations. The main components of MC simulations will be discussed in the following.

Light-tissue Interactions

For this simulation, the incoming photons arrive perpendicularly to the medium surface, each with an initial weight $W = 1$. At the surface boundary, the photon weight will be reduced equivalent to the reflected component, as

$$\Delta W = R_{sp} = \left(\frac{n_0 - n_1}{n_0 + n_1} \right)^2, \tag{2.31}$$

where n_0 and n_1 are the refractive indices of the ambient medium and the medium at the surface, respectively. The photon step size l [cm] is then calculated as

$$l = \frac{-ln(\epsilon)}{\mu_t}, \tag{2.32}$$

where ϵ is a random number in the interval [0, 1], μ_t [cm^{-1}] being the total attenuation constant $\mu_t = \mu_s + \mu_a$. On average this gives a step size equal to the mean free path μ_t^{-1}. [27] At the end of the photon step size, both scattering and absorption occurs. Here, the photon weight is reduced due to absorption and a fraction of the weight is deposited in the grid. The amount reduced is

$$\Delta W = W \frac{\mu_a}{\mu_t}, \tag{2.33}$$
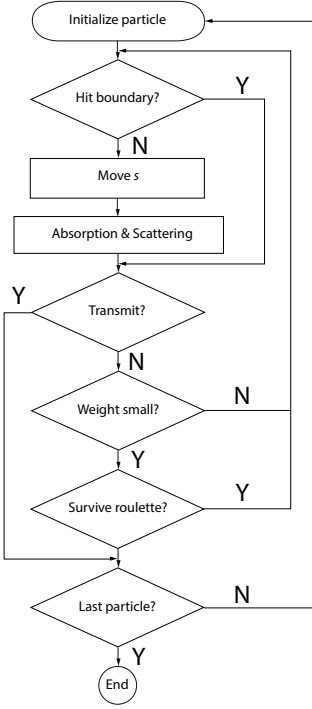
Figure 2.6: A simple flow chart for how the Monte Carlo simulations are performed.

where W is the previous weight. The new direction of the scattered photon is determined by the deflection angle Θ [0, π], and the azimuthal angle φ [0, 2π]. The deflection angle, Θ, is obtained using the Henyey-Greenstein phase function (Equation (2.8)) in combination with the randomly generated ϵ, while the azimuthal angle is simply calculated as $2\pi\epsilon$. Every time a photon reduces its weight, the fraction will be deposited in the local grid element. This will allow for a continuous reduction of energy instead of a single absorption event that terminates the photon. When the weight is sufficiently decreased due to many interaction events, further propagation will yield little useful information. However, terminating the photon would mean a loss in energy and thus the conservation of energy is not fulfilled. A method called *Russian roulette* is used, where a photon package of weight mW has one chance in m to survive. If it does not survive, the package weight is terminated and set to 0, but if it survives, the package weight is increased from W to mW. Thus the total energy is conserved.

When a photon package hits a boundary of the medium, the angle of transmittance is calculated using Snell's law,

$$n_i sin(\alpha_i) = n_t sin(\alpha_t), \tag{2.34}$$

where n_i and n_t are the refractive indices of the incident and transmitted media and α_i and α_t are the incoming and transmission angles, respectively. With a known transmission angle the reflectance is calculated by Fresnel's formula

$$R_i(\alpha_i) = \frac{1}{2} \left[\frac{sin^2(\alpha_i - \alpha_t)}{sin^2(\alpha_i + \alpha_t)} + \frac{tan^2(\alpha_i - \alpha_t)}{tan^2(\alpha_i + \alpha_t)} \right]. \tag{2.35}$$

To determine whether the photon package is reflected or transmitted, a random number ϵ is generated. If $\epsilon \leq R_i(\alpha_i)$ the package is reflected, otherwise transmitted. A logical illustration of the MC method can be seen in Figure (2.6). In conclusion, the Monte Carlo method does not require assumptions such as $\mu_s \gg \mu_a$ or other approximations, and can handle any geometry, making it an incredibly useful tool for describing transport of light. However, the accuracy of the method depends on the amount of simulated photons, making it a time consuming process. Furthermore, the parameters μ_s, μ_a and g need to be accurate in order to get a real description.

Time-of-flight Spectroscopy

If the optical parameters μ_s' and μ_a in a highly scattering sample are unknown, it is possible to obtain these with photon time-of-flight (PTOF) spectroscopy. The method is based on the principle that photons require more time to pass a highly scattering sample than a less scattering sample. By sending a short light pulse through a scattering sample, the pulse will become broadened due to the difference in photon pathlengths caused by scattering. The broadened pulse is measured using a system with high time-resolution, and will differ depending on the absorption and scattering coefficients. Thus, by fitting the shape of the broadened pulse to the photon distribution received from the diffusion approximation or Monte Carlo simulations, one may retrieve the optical properties for the chosen sample [28]. This method was used in order to receive the optical properties for the tissue phantom used for the measurements.

Upconverting Nanoparticles

Upconversion (UC) refers to the optical process of sequential absorption of two or more photons that leads to emission of light with a higher energy than the excitation photon, known as an anti-Stokes shift. The upconverting nanoparticles (UCNPs) used in this thesis are based on rare-earth ions doped in solid-state materials, that presently cause the most efficient UC process [29].

In the field of medical imaging it is common to enhance the fluorescence signal by adding an exogenous biomarker. Regularly used biomarkers include fluorescent dyes and quantum dots, which both have a Stokes-shifted emission signal. The advantage of using a biomarker with an anti-Stokes shifted emission is that the autofluorescence will be spectrally separated from the signal, due to the natural Stokes-shifted emission in tissue, causing an enormous gain in signal-to-background ratio. Furthermore, the UCNPs are insensitive to photobleaching, allowing high intensities over long periods of time without losing emission signal.

In this chapter the different processes behind upconversion will be discussed along with the power dependency of UCNPs, followed by a description of the two main UCNPs used in this work and a discussion of how to compare the two. The arguments of the upconversion mechanisms are based on the work of Auzel [4], if nothing else is specified.

3.1 Upconversion Mechanisms

Rare earth ions that are co-doped into solid state materials can be divided into two main parts responsible for upconversion, a *sensitizer* and an *activator*, which are considered having mutual interactions. The ion that absorbs the incoming light is called the *sensitizer* and the ion to which the absorbed energy is transferred to is called the *activator*. This energy transfer can be either radiative or non-radiative (Figures 3.1 and 3.2), resonant or non-resonant (Figures 3.1 and 3.3). Radiative energy transfer suggests a photon is released from the sensitizer and absorbed by the activator, while non-radiative energy transfer is through the dipole-dipole-coupling of the two ions. This makes non-radiative energy transfer extremely sensitive to distance changes between the ions, while radiative transfer is dependent on the shape of the sample. Resonant energy transfer occurs when there is no difference between the energy transmitted from the sensitizer and the energy received by the activator. Hence, a
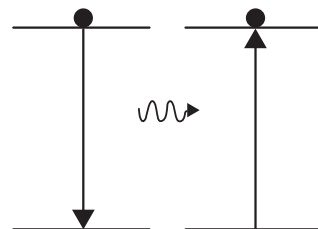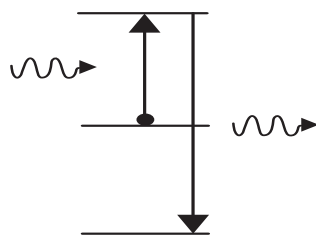

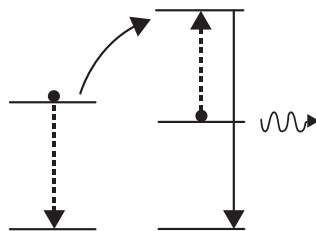**Figure 3.1:** Radiative, resonant energy transfer.
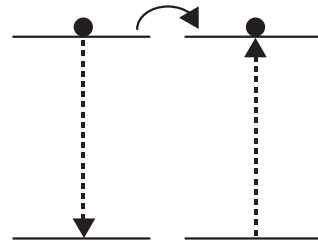
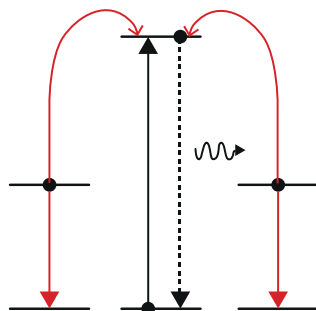**Figure 3.2:** Non-radiative, resonant energy transfer.

13
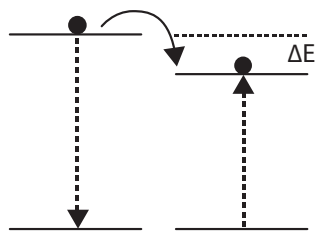
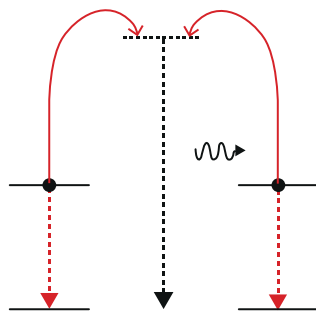**Figure 3.3:** Non-radiative, non-resonant energy transfer.

non-resonant energy transfer must be phonon-assisted in order to conserve the energy. Following are the fundamental mechanisms that cause upconversion.

3.1.1 Excited State Absorption

Excited state absorption (ESA) is an excitation process where an ion in its excited state absorbs a photon to achieve a second excited state, as seen in Figure (3.4). The probability for ESA is small.

Figure 3.4: Excited state absorption, ESA.

3.1.2 Energy Transfer Upconversion

Energy transfer upconversion (ETU) is a process involving non-radiative energy transfer between ions and is far more efficient than ESA. In the case of a sensitizer and an activator, the sensitizer first absorbs a photon. Then, the energy is transferred non-radiatively to the activator, which now enters its first excited state. A second photon is absorbed by the sensitizer and the energy is again transmitted through ETU to the activator (see Figure (3.5)), which now is in a second excited state. The activator emits a photon with higher energy than the excitation photons, i.e. upconversion has occured. As described in the section above, non-radiative energy transfer is sensitive to the distance between the ions. This means that the probability for ETU to be present will decrease with larger distances between ions. If there is an energy mismatch between the levels of the sensitizer and activator, i.e. a non-resonant energy transfer, the ETU process must be phonon assisted. Furthermore, it is possible to cover large energy mismatches by multi-phonon processes.

Figure 3.5: Energy transfer upconversion, ETU.

3.1.3 Cooperative Upconversion

There are two kinds of cooperative upconversion, namely cooperative sensitization and cooperative luminescence (Figures (3.6) and (3.7), respectively). For the first case, two sensitizers give away their energy to an activator at the same time, causing it to reach an excited state. For the second case two sensitizers emit their energy simultaneously, sending out one photon with the combined energy. Both of these processes are much less probable than ETU, since they require certain cooperative pair states in order to occur [30].

Figure 3.6: Cooperative sensitization.

3.2 Power Dependency

Due to the fact that upconversion requires two or more excitation photons in order to occur, the emission power of the UCNPs will not be linearly dependent on the excitation power. In order to describe how the emission power depends on the excitation power, a few assumptions needs to take place. A simple model of a sensitizer and an activator is used, where the sensitizer will absorb all the incoming photons and transfer a fraction of this energy to the activator. The energy level of the sensitizer matches those of the step-like activator energy levels, leading to resonant energy transfers between sensitizer and activator, see Figure (3.8). Furthermore, it is assumed that emission transitions from the activator occurs from the excited state to the ground state and that cross-

Figure 3.7: Cooperative luminescence.

relaxation processes and interexcited state emissions do not occur. Finally, only the ETU process is considered for this description. [32]

With P [1/m²s], describing the excitation photon flux, which is linearly related to power density, σ [m²] the excitation cross section for the sensitizer ion, N_g [1/m³] and τ_s [s] describing the ground state population and lifetime for the excited state in the sensitizer, respectively, the steady state condition for the excited sensitizer ions is described as [31]

$$N_s = \sigma P N_g \tau_s, \tag{3.1}$$

where N_s [1/m³] is the steady state population in the sensitizer. Note that this implies that the excitation cross section is independent of the excitation power. This model will describe the steady state population N_i of an arbitrary state $|i\rangle$ in the activator ion. W_i [m³/s] will denote the ETU rate constant from state $|i\rangle$ to $|i+1\rangle$ in the activator, and R_i [1/s] is the relaxation rate constant from state $|i\rangle$ to the ground state in the activator. Furthermore, one can see that the first excited state in the activator is proportional to the excited state in the sensitizer

$$N_1 \propto N_s. \tag{3.2}$$

This causes the first excited state in the activator to have a linear dependence to the excitation photon flux P from Equation (3.1). From here, the balance equation for the steady state population of any given state $|i\rangle$ in the activator is

$$W_{i-1} N_{i-1} N_s = (R_i + W_i N_s) N_i. \tag{3.3}$$

The processes involved are seen in Figure (3.9) and are described by: ETU from state $|i-1\rangle$ to $|i\rangle$, emission to the ground state from $|i\rangle$ and ETU from state $|i\rangle$ to $|i+1\rangle$. The steady state population of state $|i\rangle$ can be rewritten from Equation (3.3) to

$$N_i = \frac{W_{i-1} N_{i-1} N_s}{R_i + W_i N_s}. \tag{3.4}$$

In the following, the two cases of low-power excitation and high-power excitation will be discussed.

3.2.1 Low-power Limit

With a low power excitation, the upconversion process from state $|i\rangle$ to $|i+1\rangle$ can be ignored, since relaxation to the ground state will be dominant. In other words, $R_i \gg W_i N_s$, which reduces Equation (3.4) to

$$N_i = \frac{W_{i-1} N_{i-1} N_s}{R_i}. \tag{3.5}$$

The population density of state $|i\rangle$ will thus depend linearly on the population density of state $|i-1\rangle$, multiplied by the population of the excited state of the sensitizer. Since the previous state $|i-1\rangle$ can be written in a similar manner as the population of state $|i-2\rangle$ multiplied by N_s, the power dependency for low-power finally becomes

$$N_i \propto (N_s)^i \propto P^i, \tag{3.6}$$
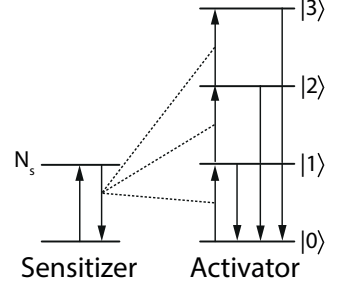
Figure 3.8: A simple model of a sensitizer and activator pair, with resonant energy levels and non-radiative energy transfer.
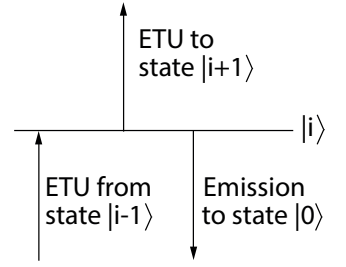
Figure 3.9: The populating and depopulating processes involved in an excited state $|i\rangle$ in the activator.

where P is the excitation photon flux, linearly related to power density, as mentioned earlier. From these results, it is clear that for a two step upconversion excitation process, the luminescence intensity will have a slope of 2 when plotted in a double logarithmic scale versus pump power. This was performed in this thesis and is described further in Chapter 4.

3.2.2 High-power Limit

For a high power excitation, the ETU process from state $|i\rangle$ to $|i+1\rangle$ will be greater than the spontaneous emission R_i, causing ETU to be the major depopulation process, i.e. $W_i N_i N_s \gg R_i N_i$. Equation (3.3), that describes the population, is thus reduced to

$$W_{i-1} N_{i-1} N_s = W_i N_i N_s. \tag{3.7}$$

This in turn has a steady state solution that is independent on the population in the excited state of the sensitizer,

$$N_i = \frac{W_{i-1}}{W_i} N_{i-1} \propto N_{i-1}. \tag{3.8}$$

The fact that $N_i \propto N_{i-1}$ allows the power dependency to be written as

$$N_i \propto N_s \propto P^1, \tag{3.9}$$

for high pump powers. Thus, plotting the luminescence from that of a high-power excitation source in a logarithmic scale, the slope will be equal to 1. It can be shown that continuously changing the pump power from low to high intensity will give a gradual change in dependency from quadratic to linear for the simple two photon upconversion process [31]. This may be used as a standard to characterize the quantum yield of UCNPs but will not be investigated further in this thesis.

3.3 Upconversion Systems

The upconverting nanoparticles generally contain sensitizer and activator ions in an inorganic host. It is important to choose these properties carefully in order to achieve high upconversion efficiency. Following there will be a description of these and how they can be varied.

3.3.1 Host Materials

The host material needs to have a good lattice structure that matches the dopant ions. In addition, the host material should have low lattice phonon energies in order to minimize nonradiative decays. This will ensure long lifetimes of the intermediate states. [33] For biomedical applications, other preferable attributes include chemical stability and biocompatibility. Finally, considering the interionic distance between activator and sensitizer ions in the host lattice is beneficial. Because of the low phonon energies in fluoride, along with its chemical stability it is frequently used as host material. A widely used combination is sodium yttrium tetrafluoride, $NaYF_4$ co-doped with sensitizer

and activator ions. It can crystallize in two phases, cubic or hexagonal, called α-NaYF$_4$ and β-NaYF$_4$ respectively. The upconverted luminescence obtained by a crystal with the hexagonal (β) phase is known to be more efficient than that from a cubic phase (α). [34] However, recently a new host material containing calcium (CaF$_2$) has been introduced, said to challenge the frequently used NaYF$_4$. Since calcium is an endogenous component in live tissue, CaF$_2$ is considered to be more biocompatible than NaYF$_4$. [35] More importantly, the CaF$_2$ promotes formation of pairs when doped with lanthanide ions, which reduces the interionic distance and in turn increases ETU processes. [36] This leads to a probable luminescence increase when using CaF$_2$ as a host material instead of NaYF$_4$, but should be examined further

3.3.2 Activator and Sensitizer

When choosing activator and sensitizer ions there are a number of points that should be taken into account [8],

1. The sensitizer ions should have a simple energy level structure, preferably with energy levels matching cost-effective laser sources.

2. The sensitizer ions should have a large absorption cross section along with a long-lived excited state.

3. The activator should have a ladder-like energy structure with long-lived excited states, and preferably the energy gaps should be similar to those of the sensitizer ions.

Furthermore, it is beneficial to choose ions that are excited and emit light in spectral regions of interest. For example, the Yb^{3+}/Tm^{3+} UCNPs with excitation at 975 nm and emission at 800 nm works well for biomedical applications since it operates within the optical window for biological tissue.

For such codoped UCNPs it is necessary to balance the amount of sensitizer ions to activator ions. A general case consists of 2 mol% activator ions and around 20 mol% sensitizer ions. By increasing the amount of doped sensitizer ions, the absorption will increase leading to enhanced upconversion emission. However, it has been reported that a high concentration of sensitizers in some systems may cause upconversion emission quenching, reducing upconversion emission. [37]
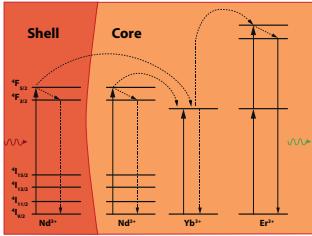
3.3.3 Core-Shell Structure

Due to the large surface to volume ratio in nanoparticles the luminescence efficiency is usually smaller than that of bulk material. [29] For lanthanide based upconversion materials, surface ligands with high-energy vibrational modes may cause quenching of the excited states. Further, if there is a high concentration of a dopant in the host lattice, such as the Yb^{3+}, energy transfer from the center of the particle to the surface, through adjacent dopant ions, may further decrease the efficiency. This may be overcome by coating the particle with an appropriate shell material. The shell should not allow any kind of energy transfer from the core to the surface of the particle. The shell should in addition contain less quenching sites than the surface of the core particle in

order to be effective. Generally there are two types of shells, active and passive. The active shell contains dopants while the passive does not. Following there will be a description of the particles that were used in this thesis.

3.4   Particles Used in this Thesis

The first observed, and very efficient, upconverting nanoparticles were Yb^{3+}/Tm^{3+} and Yb^{3+}/Er^{3+} co-doped UCNPs. These have an excitation wavelength at 975 nm and an emission at 800 nm and 650 nm, respectively. They are highly efficient when using β-$NaYF_4$ as host material. For this work, core-shell Yb^{3+}/Tm^{3+}-$NaYF_4$ UCNPs were used. The shell was passive, i.e. was not containing any sensitizer ions. For these particles, with an excitation wavelength at 975 nm, there will be a relatively high absorption due to the peak in the water absorption spectra, as seen in Figure (2.4). This leads to a rather low penetration depth along with unfavourable heat generation when used in biological tissue. [3] Recently, Yb^{3+}/Nd^{3+} co-sensitized and Er^{3+} activated UCNPs were synthesized in order to tune the excitation wavelength to a region with less water absorption in tissue. By using a core-shell structure with Nd^{3+} ions in the shell and $Nd^{3+}/Yb^{3+}/Er^{3+}$ dopants in the core, it is possible to excite the Nd^{3+} ions with 808 nm which will then transfer the energy to the second sensitizer, Yb^{3+}, in turn exciting the activator Er^{3+}. The core-shell structure and energy transfer is seen in Figure (3.10), while a clear illustration of how the energy is transferred between sensitizer and activator for the two used particles is displayed in Figure (3.11). The shell-core process described above effectively generates 650 nm emission at 808 nm excitation. The efficiency of which the energy transfers from Nd^{3+} to Yb^{3+} is around 70% [38]. The benefits of creating these modified UCNPs is that they will have a substantial decrease in water absorption due to the shift in excitation wavelength, leading to a deeper penetration and reduced heat generation for biomedical applications. Naturally there will be a reduced efficiency due to the second energy transfer step, this will, however, be compensated by the reduced water absorption at 808 nm. The work performed in this thesis is based on comparing these particles, both experimentally in tissue phantoms and by simulations in tissue and skin. The aim of the thesis is thus to suggest that using this new wavelength pair, possible with the newly synthesized particles, is beneficial for deep tissue imaging.

Figure 3.10: An illustration of the core-shell structure for the new particles. The dopants in the shell absorbs the incoming photon, which is then transferred subsequently to the core, allowing for upconversion to occur.

3.4.1   Future Outlooks

The new particles used in this work, $Nd^{3+}/Yb^{3+}/Er^{3+}$, are essentially Yb^{3+}/Er^{3+} UCNPs doped with an antenna, Nd, in a core-shell structure. This allows for Nd to absorb the incoming light at 808 nm and transfer the energy to the sensitizer, Yb, which, in combination with the activator Er, cause upconversion. This way of tuning the excitation wavelength has been evaluated further, and recently an organic infrared dye was introduced as an antenna to the upconverter Yb^{3+}/Er^{3+} [39]. The dye (IR-806) has a large absorption cross section over a broad spectral range (with a peak at 806 nm) in comparison with Yb, that has a narrow absorption spectra with a rather low cross section. This allows for more light to be absorbed and upconverted, especially when using
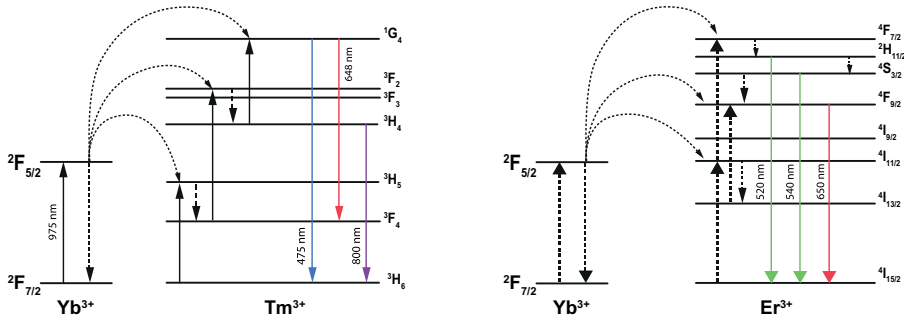
Figure 3.11: A simple energy level structure that illustrates the upconversion energy transfers involved between the sensitizer and the activator for the two combinations of RE ions, Yb^{3+}/Tm^{3+} and $(Nd^{3+})/Yb^{3+}/Er^{3+}$. Note that for our co-sensitized particles, the Yb^{3+} ion is excited by energy transfer from the Nd^{3+} ion, as seen in Figure (3.10).

a light source with a broad spectrum. The main idea with the dye-sensitized UCNPs is to implement them in solar cells to convert the low energy photons into higher energy, allowing for photovoltaics to occur. However, a large absorption increase will also benefit biomedical applications, possibly improving deep tissue imaging and signal-to-background ratio even further. The authors, Zou *et al.*, call the new particles broadband dye-sensitized UCNPs, and the phenomenon *dye-sensitized upconversion* (DUC).

Experiments and Simulations

This thesis is based on a comparison between the already well characterized and exploited Yb^{3+}/Tm^{3+} UCNPs and the recently developed $Nd^{3+}/Yb^{3+}/Er^{3+}$ co-sensitized UCNPs. The fact that two photons are required for the excitation process implies that a reduction in absorption by other chromophores in tissue will increase the fluorescence signal from the UCNPs dramatically. The newly developed UCNPs operate at a wavelength with a significantly lower absorption in tissue. This should mean a possible gain in light penetration and thus signal. As stated in Section (1.2), the main goal in this thesis was to determine that the new particles ($Nd^{3+}/Yb^{3+}/Er^{3+}$) can provide detectable signals at larger depths than the traditional particles (Yb^{3+}/Tm^{3+}). This done, it was in addition also intended to study in which tissue compositions the new particles provide a better signal than the traditional particles. This chapter includes a quick description of the materials used and the practical setup for the measurements as well as how these were performed. Thereafter the findings from the measurements will be discussed along with the simulations and their corresponding results.

4.1   Tissue Phantoms

As described in previous sections, biological tissue contains several kinds of chromophores and microscopic structures that absorb and scatter incoming light to various extent. *In vivo*, the most important chromophores are water, lipid and blood. Thus, the tissue phantoms that were created for these measurements contained water, intralipid and blood to resemble real tissue. The phantoms were created equally for both particles and contained a volume fraction of 3% blood, 3% intralipid and 94% water. The optical properties for the tissue were measured for the three significant wavelengths (650 nm, 808 nm and 975 nm) by using a photon time-of-flight spectroscopy system, briefly mentioned in Section 2.7.3. The determined optical properties can be seen in Table (4.1).

Table 4.1: Optical properties in the created tissue phantom for the significant wavelengths.

Wavelength [nm]	μ_a [cm^{-1}]	μ_s' [cm^{-1}]	μ_{eff} [cm^{-1}]
650	0.10	7.26	1.5
808	0.113	5.8	1.42
975	0.6	4.72	3.11

For this tissue phantom it is obvious that the water absorption has a large effect at the 975 nm excitation wavelength. This causes μ_{eff} at this wavelength to be greater than for the other two wavelengths, even though the reduced scattering coefficient is lower. Furthermore, optical properties at the emission wavelengths at 808 nm for the Yb^{3+}/Tm^{3+} and at 650 nm for Nd^{3+}/Yb^{3+}/Er^{3+} are quite similar, with a slight variation in reduced scattering coefficient.

4.2 Measurements

There were two fundamental measurements performed, power measurements and depth measurements. They were both performed with UCNPs in tissue phantoms and in transillumination geometry. The excitation light was guided using fibre-coupled laser diodes connected to a collimator with an appropriate band-pass filter to remove unwanted laser modes. The UCNPs were contained in an epoxy sphere with a diameter of approximately 4.5 mm each. The samples were mounted via thin plastic threads onto a metallic holder attached to two translators, allowing for vertical and horizontal variations. The emission intensity was recorded using an air-cooled CCD camera located behind appropriate filters to separate emission from excitation light. The filters were contained in an adaptor which focused the light in order to make it parallel through the filters, increasing the filters' functionality [40] [41]. The setup can be seen in Figure (4.1).
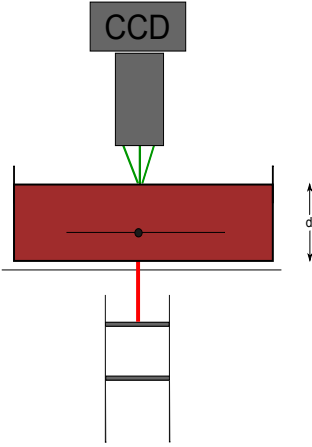

Figure 4.1: Transillumination setup used for power and depth measurements. From top to bottom: CCD-camera, adaptor containing optical filters, glass container with tissue phantom of thickness d, sample located inside tissue phantom with varying depth, and finally the collimator that was fibre-coupled to a laser diode, with a corresponding excitation band-pass filter on top.

4.2.1 Power Dependency

The upconversion process depends on several factors, described in Section (3.1). In order to compare two UCNPs with different composition accurately, it must be certain that they are both in a non-saturated region when measurements are performed. As described in Section (3.2), the emission is poportional to the excitation power squared. Thus, it is necessary to find the saturation range where increasing the power by a factor of 2 gives a 4 times stronger emission.

This was performed for both particles by placing them in a tissue phantom at a depth from the excitation side of 3 mm, while varying the excitation power. The emission signal was recorded with the CCD camera and for each image the background was subtracted. The emission signal was plotted in a double logarithmic scale as a function of excitation intensity to find a slope equal to 2, see Figure (4.2). The excitation intensity in this non-saturated region was subsequently used for the depth measurement series.
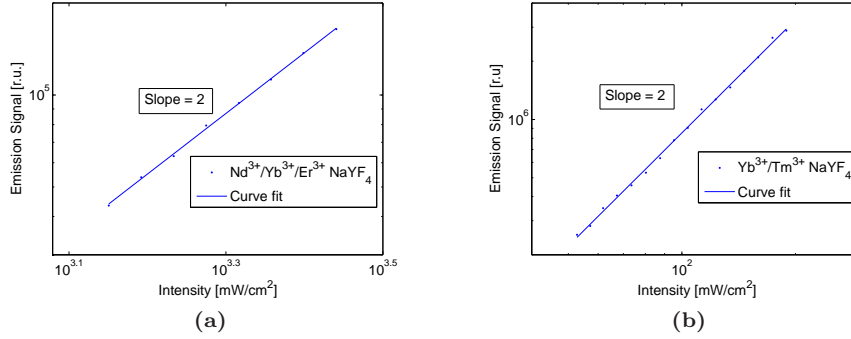
Figure 4.2: Power dependency measurements for the two particles used in this work, (a) $Nd^{3+}/Yb^{3+}/Er^{3+}$ co-sensitized UCNPs and (b) Yb^{3+}/Tm^{3+} UCNPs. Both in a non-saturated regime with a slope = 2.

4.2.2 Depth Measurements

When it was certain that the UCNPs were not saturated, a depth comparison was carried out. Measurements started at a depth of 3 mm, with excitation intensities decided from the power measurements described above. The depth was increased with a step size of 0.5 mm until a total depth of 10 mm was reached. For each step an image was acquired and the background was subtracted. The emission was normalized to the first point at 3 mm and plotted as a function of depth. The change in signal for the two particles investigated (one containing UCNPs doped with Yb^{3+}/Tm^{3+} and the other with $Nd^{3+}/Yb^{3+}/Er^{3+}$) can be seen in Figure (4.3) .
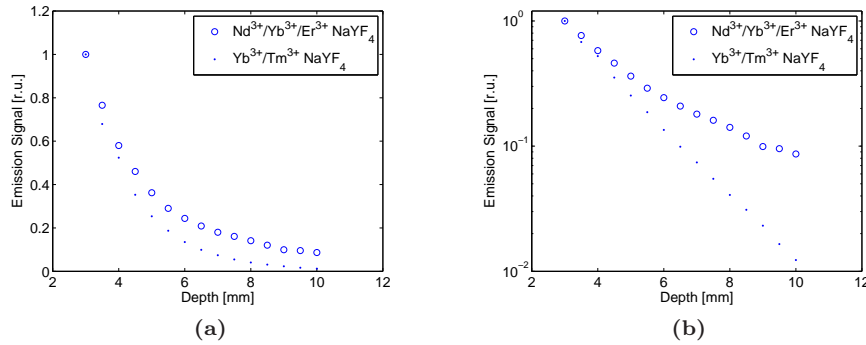
Figure 4.3: Normalized emission intensity as a function of depth in (a) linear scale and (b) semilogarithmic scale.

4.3 Discussion of Experimental Results

From the power dependency measurements, it is certain that the particles are in a non-saturated region as the slope = 2. Since the excitation intensity will decrease with increasing depth, the particles will stay in a non-saturated region. For the depth measurements, as is noted in Figure (4.3), the signal from the

traditional Yb^{3+}/Tm^{3+} UCNPs decreases faster than the signal from the new particles. In the logarithmic scale we see that at a depth of 10 mm the signal is almost one order of magnitude stronger. This proves that the new particles will allow for deeper penetration as well as reduced heat generation due to the reduced absorption.

4.4   Simulations

From the depth measurements it was noticed that the new particles showed a considerable gain of the detected signal at larger depths for the chosen tissue phantom. In order to verify the results, several simulations were performed. The diffusion approximation and Monte Carlo simulations described in Sections (2.7.2) and (2.7.3) were used to compare theoretical values with measured results. A second goal with the simulations was to determine for which combination of chromophores in the tissue the new particles had a considerable gain.

4.4.1   Diffusion Approximation

The diffusion approximation is derived off the radiative transfer equation and may be used to describe the fluence rate in a medium with known optical properties [5]. The emission signal generated locally is related to this fluence rate. For the case of upconversion, the strength of the locally emitted light is proportional to the fluence rate squared. This multiplied with the fluence rate of the emission (representing the probablity for the emitted light to reach the detector) leads to an approximation of the detectable signal as a function of depth. With the optical properties measured from the photon-time of flight system it was possible to express the signal as

$$\phi \propto \frac{e^{-2\mu_{effexc}\mathbf{r}}}{\mathbf{r}^2} \cdot \frac{e^{-\mu_{effem}(d-\mathbf{r})}}{d-\mathbf{r}}, \tag{4.1}$$

where d is the thickness of the phantom, $\mathbf{r}$ is the depth of the sample measured from the excitation side, and μ_{effexc}, μ_{effem} represent the effective attenuation coefficient for the excitation and emission light, respectively. Since the expression was normalized, in accordance with the depth measurements, the constants shown in Equation (2.25) are not included. Due to the fact that the samples had a rather large diameter of 4.5 mm, an offset of the r-parameter was optimized for each particle series to fit the approximation to the measured signal as well as possible. Figure (4.4) shows the diffusion approximation for the two samples along with the corresponding residual.

4.4.2   Monte Carlo Simulations

Although the diffusion approximation agreed well to the measured values, it is not quite reasonable to use the infinite diffusion approximation for a finite tissue phantom. Thus, Monte Carlo simulations were also performed. By simulating a large number of photons in a similar manner as described in section (2.7.3) it is possible to get the fluence distribution for a tissue with desired optical properties. The emission signal was described by the excitation
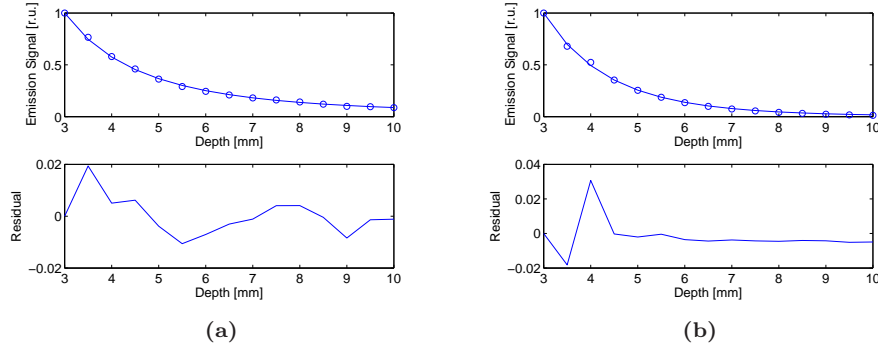
Figure 4.4: Expression from diffusion approximation with optical properties equal to the tissue phantom, fitted to the measured values for (a) $Nd^{3+}/Yb^{3+}/Er^{3+}$, and (b) Yb^{3+}/Tm^{3+}. The bottom graph shows the residual for that particle. The offset values were calculated to 0.58 mm and 2.9 mm, for (a) and (b) respectively.

fluence squared times the emission fluence, similar to what is described above. With an evaluated fluence distribution the emission signal was compared to the measured values. The comparison is seen in Figure (4.5).
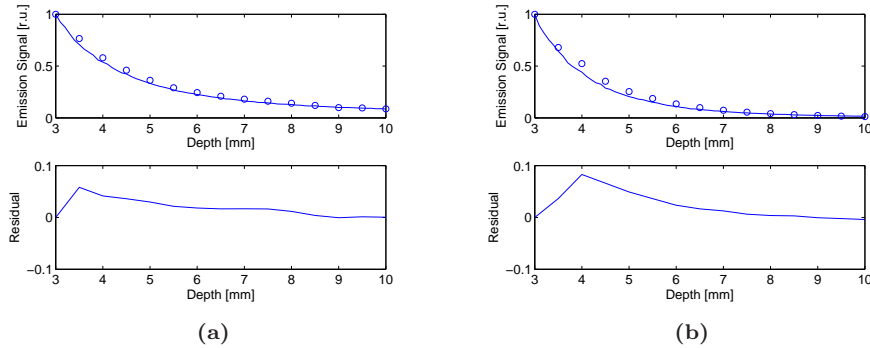

Figure 4.5: Monte Carlo simulations with values for optical properties calculated by adding volume fractions of known chromophores. For comparison, the measured data for (a) $Nd^{3+}/Yb^{3+}/Er^{3+}$, and (b) Yb^{3+}/Tm^{3+} are added with their respective residuals.

For this simulation, the size of the samples were taken into account in a similar manner as in the diffusion approximation. Furthermore, the measured optical properties were not used, instead the contribution from each chromophore (spectrum seen in Figure (2.4)) was added by using the same volume fraction as the tissue phantom used for the measurements. This is beneficial, since it allows for variations in the volume fractions, making it possible to simulate any kind of tissue composition.

Lipid

Further simulations were performed and a variation of lipid was studied. The signal gain, i.e. the signal ratio of $Nd^{3+}/Yb^{3+}/Er^{3+}$ over Yb^{3+}/Tm^{3+}, was extracted and the result is seen in Figure (4.6). Here, the size of the samples were not taken into account. Thus, we approximate for samples that are perfect
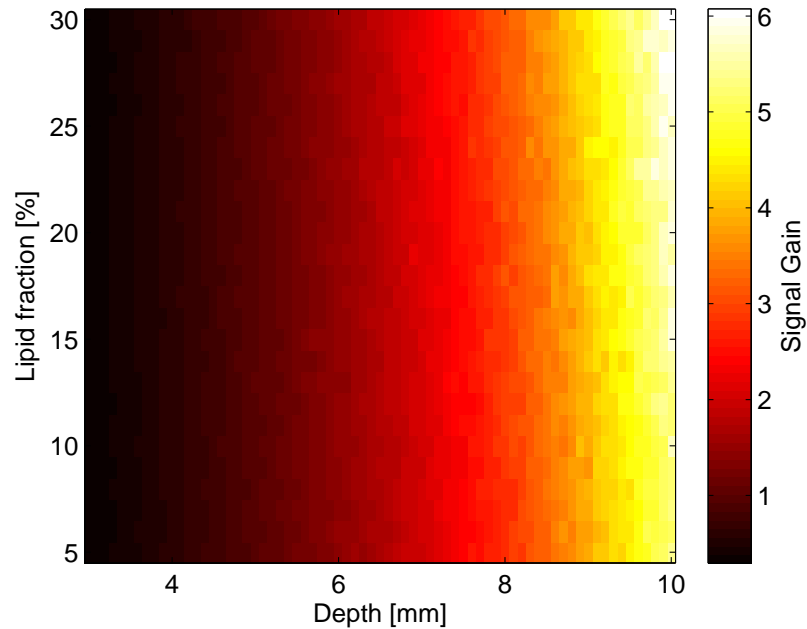
Figure 4.6: Monte Carlo simulation with a variation of lipid volume fraction. The gain is plotted as a function of depth.

point sources. The lipid volume fraction was varied from 5% - 30% while the blood fraction was constant at 5% with a 75% saturation, leaving the water fraction to vary from 90% - 65%. As is noted, the gain does not vary much depending on lipid fraction in the tissue.

Blood

A second series of simulations were conducted for blood variation (Figure (4.7)). Here, the lipid was constant at 15% while the blood fraction varied from 1% - 30%, again with a saturation of 75%, giving water a volume fraction of 84% - 55%. Notable is that the gain quickly decreases as the blood volume increases. This is most likely due to the fact that the 650 nm emission light from $Nd^{3+}/Yb^{3+}/Er^{3+}$ is greatly absorbed by the non-oxygenated haemoglobin (see Figure (2.4)).

Melanin

Finally, in order to evaluate a realistic in vivo measurement, a thin layer of melanin was added in front of the tissue to simulate skin. The layer was 0.1 mm thick and had a varying melanin concentration of 1% - 45% with a constant blood and lipid concentration of 3% each. The remaining volume fraction consisted of water. The tissue after the melanin layer contained 5% blood, 15% lipid and 80% water. The gain result can be seen in Figure (4.8).
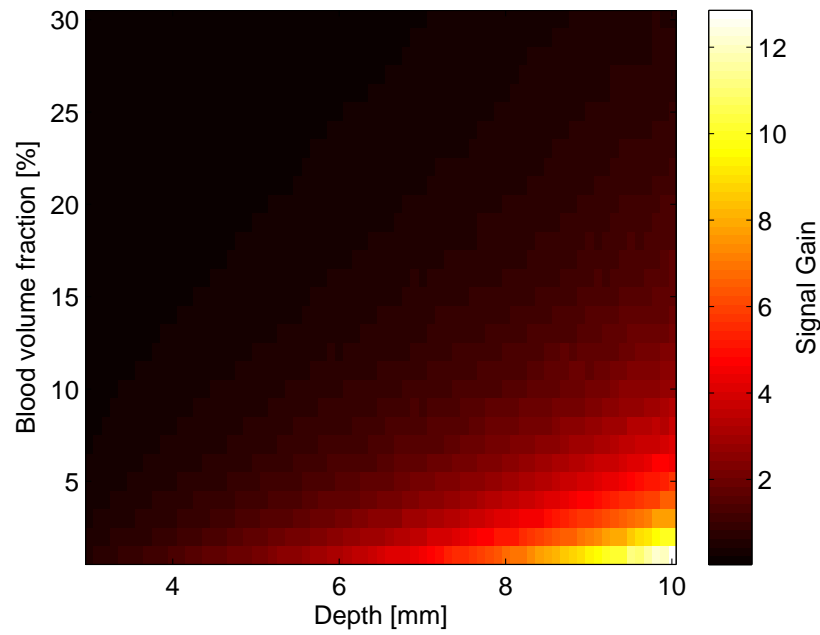
Figure 4.7: Monte Carlo simulation with a variation of blood volume fraction. The gain is plotted as a function of depth.
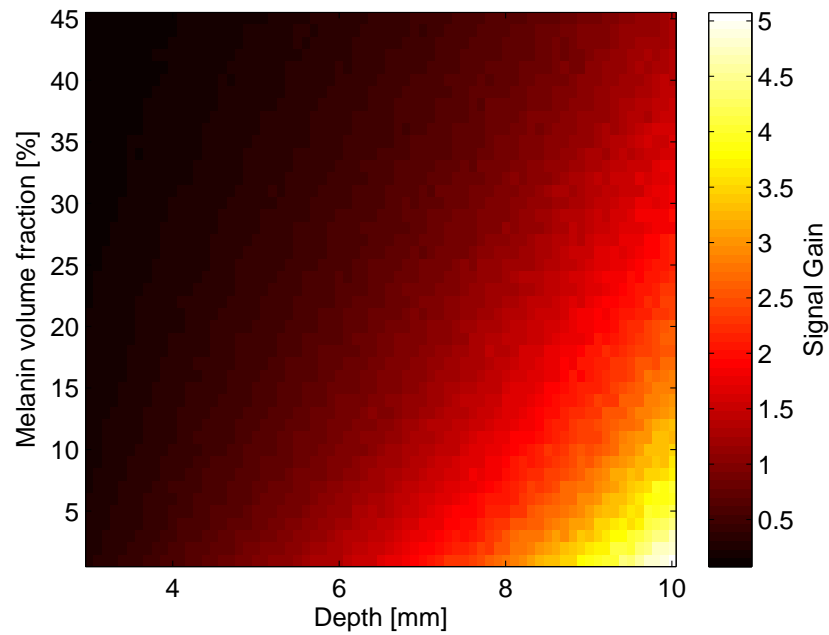
Figure 4.8: Monte Carlo simulation with a varying melanin layer in front of a constant tissue. The gain is plotted as a function of depth.

4.5   Discussion of Results of Simulations and Diffusion Approximation

The diffusion approximation showed good agreement with the experimental values after the fit. As a result, one can understand that the size of the sample is significant to the depth measurements. The extra distance values were calculated to be 0.58 mm for the new particles and 2.9 mm for the traditional particles. Since the total diameters were $\approx$ 4.5 mm for both spheres these added values are reasonable. For the Monte Carlo simulations the different chromophores were varied in order to determine the optimal tissue composition for the new particles. As is seen in Figure (4.6), the lipid fraction did not have a large impact on gain. However, it results in a slightly larger gain for higher lipid fractions (a gain of 6 for 30% lipid compared to a gain of 5 for 5% lipid at 10 mm depth). For the simulation with blood variation (Figure (4.7)) it is noted that a large blood fraction leads to a decrease in gain. At a volume fraction of 1% blood the gain is larger than 12, while at a volume fraction of 5% it is decreased to $\approx$ 5 (both considered at a depth of 10 mm). For the final simulation, with melanin, seen in Figure (4.8), the gain at 10 mm depth decreases relatively quickly. At a melanin volume fraction of 1% the gain is slightly larger than 5, while at a volume fraction of 20% the gain is close to 2.5.

Concluding Remarks and Outlook

This thesis presents a thorough comparison between two different upconverting nanocrystals in different aspects. Since studies from the past already has shown that autofluorescence free imaging is possible by using UCNPs [2], this has not been a major focus of the thesis. The main goal was to determine how well the newly co-sensitized $Nd^{3+}/Yb^{3+}/Er^{3+}$ UCNPs function in comparison with traditional and intensely studied Yb^{3+}/Tm^{3+}. For the sake of the reader, in this discussion the UCNPs will be termed the new, and the traditional UCNPs, respectively.

The practical depth measurements show that in a non-saturated regime the new particles have a rather large (almost one order of magnitude) signal gain at a depth of 10 mm. This suggests that the new particles provide means for imaging at larger depths and consequently, due to lower absorption, also reduce heat generation in tissue. Furthermore, the experimental measurements were theoretically verified by using the diffusion approximation and MC simulations. The results show a good agreement which supports the proposition further. The MC simulations also show that for different kinds of tissue composition containing blood, fat and water, the signal gain is still rather large. For an increased blood concentration the gain decreases due to the large absorption from non-oxygenated blood at the emission wavelength from the new particles, as mentioned in Section (4.4.2). However, this is not a large issue, since tissue with large amounts of blood, such as liver tissue, contains around 5% blood [42]. Finally, for the simulations with a melanin layer, the reduction is substantial for high values. The natural increase in absorption for shorter wavelength, due to the fact that melanin is a way to protect us from harmful UV-light from the sun, causes the new particles to lose signal. However, according to Jacques [43], the volume fraction of melanin in skin for light skinned caucasians varies between 1-3%, which according to the MC simulations still provides up to 5 times larger gain. In addition, for the melanin simulation, the blood volume fraction was set to 5%, which as mentioned above is a large value that adds to the loss in signal.

From the power dependency measurements, it is noted that the power required to acquire a non-saturated regime for the traditional UCNPs is considerably lower than that used for the new UCNPs. In general, the new UCNPs had a substantially lower emission than the traditional UCNPs. This is explained by the fact that the core-shell structure that was intended for the new

UCNPs was not entirely achieved during synthesization. Thus, shell particles were loosely distributed in the sample, absorbing photons without redistributing the energy. In addition, there is an energy loss due to the energy transfer step to the second sensitizer for the new particles, compared to the traditional ones, leading to a natural decrease in efficiency. Due to the fact that the particles were not perfectly synthesized, additional measurements should be performed, preferably *in vivo* to be able to determine how much the melanin in skin actually reduces signal.

In conclusion, I believe that the new particles, when synthesized accordingly, very well may replace the traditional particles for most applications. The downside of the new particles would be if there are large amounts of melanin to absorb the excitation and emission light. Since water is the largest part of biological tissue, it is necessary to optimize the contrast agents in order to maximize the signal. Due to the results obtained from this work, the new particles are shown to provide higher sensitivity at large depths for certain tissues. These newly developed upconverting nanoparticles may thus very well lead us one step closer to finding the most optimal tools for biomedical applications.

Personal Reflections

During this project, a large portion was dedicated to practical measurements. Thus, difficult challenges have been to arrange optimal measuring techniques that has put my theoretical knowledge and creativity to the test. Working alone has forced me to take responsibility in the search for errors in measurements and simulations, which has taught me to think in an analytical and logical way, as well as the importance of discussing with others. Furthermore, it has taught me to write in a scientific manner and of course, given me insight in a very interesting research topic.

Acknowledgements

First of all, I would like to thank my principal supervisor, Professor Stefan Andersson-Engels for allowing me this project as well as being a part of the biophotonics group. You have always been supportive and positive whenever I have encountered problems in my project. Your ways of teaching, guiding and participating in various projects is a true inspiration.

Furthermore, I would like to thank my co-supervisor and mentor Haichun Liu, who has always been there for me when I needed guidance or someone to discuss with. Can Xu, my second co-supervisor, has also been of great help during all stages of the project. Together, the two of you have provided fruitful discussions and support when it was most needed.

Special thanks goes also to Arefeh Mousavi, who has collaborated with me during experiments and provided the project with a much needed adaptor. Björn Thomasson, who has arrived early hours to assist me in the lab - your passion for science is inspirational. And of course Sören Johansson and Staffan Strömblad, who patiently assisted me with time-of-flight measurements on my tissue-phantoms.

Finally I would like to thank everyone in my work surroundings, Nina Reistad, David and Therese, Haiyan Xie and Dmitry Khoptyar, it has been a pleasure to come in and spend time every day with everyone in here.

Bibliography

[1] M. Monici, "Cell and tissue autofluorescence research and diagnostic applications," *Biotechnology annual review*, vol. 11, pp. 227–256, 2005.

[2] C. T. Xu, N. Svensson, J. Axelsson, P. Svenmarker, G. Somesfalean, G. Chen, H. Liang, H. Liu, Z. Zhang, and S. Andersson-Engels, "Autofluorescence insensitive imaging using upconverting nanocrystals in scattering media," *Applied Physics Letters*, vol. 93, no. 17, p. 171103, 2008.

[3] Q. Zhan, J. Qian, H. Liang, G. Somesfalean, D. Wang, S. He, Z. Zhang, and S. Andersson-Engels, "Using 915 nm laser excited $tm^{3+}/er^{3+}/ho^{3+}$-doped $naybf_4$ upconversion nanoparticles for in vitro and deeper in vivo bioimaging without overheating irradiation," *ACS nano*, vol. 5, no. 5, pp. 3744–3757, 2011.

[4] F. Auzel, "Upconversion and anti-stokes processes with f and d ions in solids," *Chemical reviews*, vol. 104, no. 1, pp. 139–174, 2004.

[5] L. V. Wang and H.-i. Wu, *Biomedical optics: principles and imaging*. John Wiley & Sons, 2012.

[6] C. F. Bohren and D. R. Huffman, *Absorption and scattering of light by small particles*. John Wiley & Sons, 2008.

[7] F. H. Perrin, "Whose absorption law?," *JOSA*, vol. 38, no. 1, pp. 72–74, 1948.

[8] H. Liu, *Advancing Upconversion Emissions for Biomedical Imaging*. PhD thesis, Lund University, 2014.

[9] F. A. Jenkins and H. E. White, *Fundamentals of physical optics*. 1937.

[10] J. W. S. B. Rayleigh, *On the scattering of light by small particles*. 1871.

[11] G. Mie, "Beiträge zur optik trüber medien, speziell kolloidaler metallösungen," *Annalen der physik*, vol. 330, no. 3, pp. 377–445, 1908.

[12] L. G. Henyey and J. L. Greenstein, "Diffuse radiation in the galaxy," *The Astrophysical Journal*, vol. 93, pp. 70–83, 1941.

[13] S. L. Jacques and S. A. Prahl, "Biomedical optics." HTTP://OMLC.OGI.EDU/EDUCATION/ECE532/CLASS3/MUSP.HTML, 1998.

[14] G. M. Hale and M. R. Querry, "Optical constants of water in the 200-nm to 200-μm wavelength region," *Applied optics*, vol. 12, no. 3, pp. 555–563, 1973.

[15] S. Prahl, "Optical absorption of hemoglobin," 1999.

[16] R. L. van Veen, H. Sterenborg, A. Pifferi, A. Torricelli, and R. Cubeddu, "Determination of vis-nir absorption coefficients of mammalian fat, with time-and spatially resolved diffuse reflectance and transmission spectroscopy," p. SF4, 2004.

[17] S. L. Jacques, R. D. Glickman, and J. A. Schwartz, "Internal absorption coefficient and threshold for pulsed laser disruption of melanosomes isolated from retinal pigment epithelium," pp. 468–477, 1996.

[18] R. Weissleder and V. Ntziachristos, "Shedding light onto live molecular targets," *Nature medicine*, vol. 9, no. 1, pp. 123–128, 2003.

[19] A. Pifferi, R. van Veen, H. Sterenborg, A. Torricelli, E. Chikoidze, and R. Cubeddu, "Determination of visible near-ir absorption coefficients of mammalian fat using time-and spatially resolved diffuse reflectance and transmission spectroscopy," *Journal of biomedical optics*, vol. 10, no. 5, pp. 054004–054004, 2005.

[20] S. L. Jacques, "Melanosome absorption coefficient." HTTP://OMLC.OGI.EDU/SPECTRA/MELANIN/MUA.HTML, 1998.

[21] V. V. Tuchin and V. Tuchin, *Tissue optics: light scattering methods and instruments for medical diagnosis*, vol. 642. SPIE press Bellingham, 2007.

[22] G. Marriott, R. M. Clegg, D. J. Arndt-Jovin, and T. M. Jovin, "Time resolved imaging microscopy. phosphorescence and delayed fluorescence imaging.," *Biophysical journal*, vol. 60, no. 6, p. 1374, 1991.

[23] M. v. van Rossum and T. M. Nieuwenhuizen, "Multiple scattering of classical waves: microscopy, mesoscopy, and diffusion," *Reviews of Modern Physics*, vol. 71, no. 1, p. 313, 1999.

[24] D. Contini, F. Martelli, and G. Zaccanti, "Photon migration through a turbid slab described by a model based on diffusion approximation. i. theory," *Applied optics*, vol. 36, no. 19, pp. 4587–4599, 1997.

[25] N. Svensson and C. Xu, "Upconverting luminescence imaging and tomography for biomedical applications," Master's thesis.

[26] H. Liu, *Advancing upconversion emission for biomedical imaging.* PhD thesis, Division of Atomic Physics, Faculty of Engineering, LTH, Lund University, 2014.

[27] L. Wang and S. L. Jacques, "Monte carlo modeling of light transport in multi-layered tissues in standard c," *The University of Texas, MD Anderson Cancer Center, Houston*, 1992.

[28] T. Svensson, *Pharmaceutical and biomedical applications of spectroscopy in the photon migration regime.* PhD thesis, Lund University, 2008.

[29] M. Haase and H. Schäfer, "Upconverting nanoparticles," *Angewandte Chemie International Edition*, vol. 50, no. 26, pp. 5808–5829, 2011.

[30] T. Miyakawa and D. L. Dexter, "Cooperative and stepwise excitation of luminescence: Trivalent rare-earth ions in yb^{3+}-sensitized crystals," *Phys. Rev. B*, vol. 1, pp. 70–80, Jan 1970.

[31] H. Liu, C. T. Xu, D. Lindgren, H. Xie, D. Thomas, C. Gundlach, and S. Andersson-Engels, "Balancing power density based quantum yield characterization of upconverting nanoparticles for arbitrary excitation intensities," *Nanoscale*, vol. 5, no. 11, pp. 4770–4775, 2013.

[32] J. Suyver, A. Aebischer, S. García-Revilla, P. Gerner, and H. Güdel, "Anomalous power dependence of sensitized upconversion luminescence," *Physical Review B*, vol. 71, no. 12, p. 125123, 2005.

[33] J. Van Dijk and M. Schuurmans, "On the nonradiative and radiative decay rates and a modified exponential energy gap law for 4f–4f transitions in rare-earth ions," *The Journal of Chemical Physics*, vol. 78, no. 9, pp. 5317–5323, 1983.

[34] J. Suyver, J. Grimm, M. Van Veen, D. Biner, K. Krämer, and H. Güdel, "Upconversion spectroscopy and properties of $nayf_4$ doped with er^{3+}, tm^{3+} and/or yb^{3+}," *Journal of Luminescence*, vol. 117, no. 1, pp. 1–12, 2006.

[35] J. Shen, G. Chen, T. Y. Ohulchanskyy, S. J. Kesseli, S. Buchholz, Z. Li, P. N. Prasad, and G. Han, "Tunable near infrared to ultraviolet upconversion luminescence enhancement in (α-$nayf_4$: Yb, tm)/caf_2 core/shell nanoparticles for in situ real-time recorded biocompatible photoactivation," *Small*, vol. 9, no. 19, pp. 3213–3217, 2013.

[36] N.-N. Dong, M. Pedroni, F. Piccinelli, G. Conti, A. Sbarbati, J. E. Ramírez-Hernández, L. M. Maestro, M. C. Iglesias-de la Cruz, F. Sanz-Rodriguez, A. Juarranz, *et al.*, "Nir-to-nir two-photon excited caf_2: Tm^{3+}, yb^{3+} nanoparticles: multifunctional nanoprobes for highly penetrating fluorescence bio-imaging," *ACS nano*, vol. 5, no. 11, pp. 8665–8671, 2011.

[37] F. Vetrone, J.-C. Boyer, J. A. Capobianco, A. Speghini, and M. Bettinelli, "Significance of yb^{3+} concentration on the upconversion mechanisms in codoped y_2o_3: Er^{3+}, yb^{3+} nanocrystals," *Journal of Applied Physics*, vol. 96, no. 1, pp. 661–667, 2004.

[38] Y.-F. Wang, G.-Y. Liu, L.-D. Sun, J.-W. Xiao, J.-C. Zhou, and C.-H. Yan, "Nd^{3+}-sensitized upconversion nanophosphors: efficient in vivo bioimaging probes with minimized heating effect," *ACS nano*, vol. 7, no. 8, pp. 7200–7206, 2013.

[39] W. Zou, C. Visser, J. A. Maduro, M. S. Pshenichnikov, and J. C. Hummelen, "Broadband dye-sensitized upconversion of near-infrared light," *Nature Photonics*, vol. 6, no. 8, pp. 560–564, 2012.

[40] B. Zhu, J. C. Rasmussen, Y. Lu, and E. M. Sevick-Muraca, "Reduction of excitation light leakage to improve near-infrared fluorescence imaging for tissue surface and deep tissue imaging," *Medical physics*, vol. 37, no. 11, pp. 5961–5970, 2010.

[41] B. Zhu, J. C. Rasmussen, Y. Lu, and E. M. Sevick-Muraca, "Reduction of noise floor for molecular, fluorescence-enhanced optical imaging," pp. 789104–789104, 2011.

[42] R. Nachabé, D. J. Evers, B. H. Hendriks, G. W. Lucassen, M. van der Voort, J. Wesseling, and T. J. Ruers, "Effect of bile absorption coefficients on the estimation of liver tissue optical properties and related implications in discriminating healthy and tumorous samples," *Biomedical optics express*, vol. 2, no. 3, pp. 600–614, 2011.

[43] S. Jacques, "Optical absorption of melanin."